Available online at www.sciencedirect.com

ScienceDirect

Acta Materialia 61 (2013) 7767–7780

Acta MATERIALIA

www.elsevier.com/locate/actamat

# Laser compression of nanocrystalline tantalum

C.H. Lu [a], B.A. Remington [b], B.R. Maddox [b], B. Kad [a], H.S. Park [b], M. Kawasaki [c,d], T.G. Langdon [d,e], M.A. Meyers [a,*]

[a] University of California, San Diego, La Jolla, CA 92093, USA
[b] Lawrence Livermore National Laboratory, Livermore, CA 94550, USA
[c] Division of Materials Science and Engineering, Hanyang University, 17 Haengdang-dong, Seongdong-gu, Seoul 133-791, South Korea
[d] Departments of Aerospace & Mechanical Engineering and Materials Science, University of Southern California, Los Angeles, CA 90089-1453, USA
[e] Materials Research Group, Faculty of Engineering and the Environment, University of Southampton, Southampton SO17 1BJ, UK

Received 10 July 2013; received in revised form 6 September 2013; accepted 8 September 2013
Available online 5 October 2013

## Abstract

Nanocrystalline tantalum (grain size ~70 nm) prepared by severe plastic deformation (high-pressure torsion) from monocrystalline [1 0 0] stock was subjected to shock compression generated by high-energy laser (~350–850 J), creating pressure pulses with initial duration of ~3 ns and amplitudes of up to ~145 GPa. The laser beam, with a spot radius of ~1 mm, created a crater of significant depth (~135 μm). Transmission electron microscopy revealed few dislocations within the grains and an absence of twins at the highest shock pressure, in contrast with monocrystalline tantalum. Hardness measurements were conducted and show a rise as the energy deposition surface is approached, evidence of shock-induced defects. The grain size was found to increase at a distance of 100 μm from the energy deposition surface as a result of thermally induced grain growth. The experimentally measured dislocation densities are compared with predictions using analyses based on physically based constitutive models, and the similarities and differences are discussed in terms of the mechanisms of defect generation. A constitutive model for the onset of twinning, based on a critical shear stress level, is applied to the shock compression configuration. The predicted threshold pressure at which the deviatoric component of stress for slip exceeds the one for twinning is calculated and it is shown that it is increased from ~24 GPa for the monocrystalline to ~150 GPa for the nanocrystalline tantalum (above the range of the present experiments). Calculations using the Hu–Rath analysis show that grain growth induced by the post shock-induced temperature rise is consistent with the experimental results: grains grow from 70 to 800 nm within the post-shock cooling regime when subjected to a laser pulse with energy of 684 J.

*Keywords:* Dislocations; High-pressure torsion; Laser treatment; Tantalum; Shock compression

## 1. Introduction

The experimental use of lasers to study high-pressure states in fluids can be dated from 1963 [1]. Shortly thereafter, pulsed lasers were used to investigate shock-wave propagation [2]. Early laser experiments showed a variety of applications. In the 1980s, it was demonstrated that laser shock pulses can harden aluminum alloys significantly [3,4]. White [5,6] and others [7–9] introduced the use of lasers to obtain Hugoniot data over a broad range of pressures. Cottet et al. [10] studied the effects of shock-wave propagation in Al, Cu and Au.

A systematic inquiry into the effects of laser pulses on face-centered cubic (fcc) metals (Cu and Cu–Al) was initiated in 2001 by our group [11–15] and has yielded significant results that have been explained in terms of shock compression. This work was extended to monocrystalline nickel [16], nanocrystalline nickel [17], laminated Ni/Al material [18,19], vanadium [20] and monocrystalline tantalum [21]. Loomis et al. [22–24] have investigated the extreme response of NiAl bicrystals.

---

* Corresponding author.
*E-mail address:* mameyers@ucsd.edu (M.A. Meyers).

1359-6454/$36.00 © 2013 Acta Materialia Inc. Published by Elsevier Ltd. All rights reserved.
http://dx.doi.org/10.1016/j.actamat.2013.09.016

For Cu, the structures varied from dislocation cells at low pressures to stacking faults at intermediate pressures, to twins at higher pressures; the threshold pressure for twinning was 30 GPa for [1 0 0] and 40 GPa for [1 3 4]. This pressure was clearly dependent on crystalline orientation. For Cu–Al alloys, the decrease in stacking-fault energy produced a decrease in the threshold twinning stress.

Laser-driven shocks are different from shocks launched by plate impact methods. The cooling rate in laser-driven shocks is much higher, due to the decay of the wave, enabling recovery of the deformation structure, with minimal post-shock annealing. In addition, phenomena that have temporal and spatial scales larger than the drive pulse duration and length (such as shear bands) are not present. This has been shown by Cao et al. [25] and quantified by Bourne [26] as the Freya number, a critical parameter establishing the condition for different deformation processes.

Nanocrystalline refractory metals have received considerable attention due to their high mechanical strength [27]. The mechanisms of plastic deformation (slip, twinning) in the high-pressure, high-strain-rate regimes enabled by laser energy deposition are still not well understood, especially for nanocrystalline metals. The regimes obtained by laser-induced compression are indeed extreme and cannot be accessed by other experimental methods. The objective of this study is to examine the residual defects resulting from laser-driven shock compression of nanocrystalline Ta. For Ni, it was demonstrated that grain sizes affect the average dislocation density, slip–twinning transition shock pressure and the sensitivity of the twinning deformation substructure [16]. Thus, significant differences in the deformation response are also expected for body-centered cubic (bcc) metals.

## 2. Experimental techniques

Nanocrystalline Ta was prepared by high-pressure torsion (HPT) processing from [1 0 0] monocrystalline Ta. Pure monocrystalline Ta was obtained from MarkeTech Intl, Inc. The interstitial content (wt. ppm) for the monocrystalline Ta was analyzed as O: <10, N: <10, H: 7.6 and C: <10 by standard secondary ion mass spectrometry at the Evans Analytical Group. The reason for using monocrystalline Ta as the starting material was to ensure that the composition was identical to that of the previously studied monocrystalline Ta, thus enabling a direct comparison [21].

Processing by HPT was conducted at room temperature using a quasi-constrained HPT facility (Fig. 1a) with upper and lower anvils having a cylindrical depression at the center of adjacent surfaces with a depth of 0.25 mm and a diameter of 10 mm [28]. The sample (3 mm diameter and 3 mm thick) was placed in the depression on the lower anvil. This anvil was brought into position so that the disc received severe compressive pressure. All samples were processed at a pressure of 6 GPa for a total of six turns at a rotational speed of 1 rpm. HPT processing causes the disk dimensions to change to ~10.5 mm diameter × 0.75 mm thick with some outflow around the periphery as visible in Fig. 1b (lower). The microhardness increases from the center of the disc and becomes uniform after a radius of ~0.5 mm (Fig. 1b, upper). Five small discs (3 mm diameter × 0.6 mm height, dashed circles in Fig. 1b) were cut from the peripheral part of the thinner Ta by electric discharge machining. The microhardness measurements indicate that the samples were cut from the uniform region. Five specimens were stacked into a polycrystalline Ta cylinder, and a momentum trap was used at the back as shown by the assembly in Fig. 1c. The function of these lateral and bottom momentum traps is to ensure that the reflected waves are trapped and that one single pulse traverses the specimens. The necessity of these momentum traps has been demonstrated by DeCarli and Meyers [29], Gray [30,31] and Bourne [32] for gas-gun and explosively loaded systems. In laser compression, the duration of the pulse is lower by 2–3 orders of magnitude and the wave therefore decays much more rapidly. Nevertheless, the use of these momentum traps is recommended, if experimentally feasible.

The laser recovery experiments were performed at the Laboratory for Laser Energetics, University of Rochester (Omega Facility). The laser compression experiments designed for recovery used a ramp loading enabled by a reservoir in front of the assembly (Fig. 1d). The formation of the plasma in the gap between the polycarbonate ablator and sample assembly (reservoir) leads to quasi-isentropic loading with a temperature rise significantly lower than shock compression. However, the effect dissipates over a distance of 42 μm [21]. The recovery set-up, shown in Fig. 1d, has been thoroughly tested for recovery of fcc metals [11] and Ta [21]. The Ta target (Fig. 1c), with dimensions of 5 mm diameter × 5 mm height, was placed behind a Ta washer, inside a stainless steel recovery container. The inside of this container was filled with Aerogel which acts as a deceleration medium for the Ta targets after laser compression. The recovery container was designed to fit into the Omega chamber. The detailed recovery experimental set-up is described by Lu et al. [21]. The targets were successfully recovered in this geometry. The Aerogel introduced no additional damage into the recovered samples and acted as a medium for gradual deceleration.

The 1-D LASNEX simulation of temperature as a function of time at different depths into the Ta yielded a very narrow region in which the loading was quasi-isentropic. This transition from quasi-isentropic to shock compression is clearly defined by a characteristic decrease in rise time and an increase in temperature [21]. The quasi-isentropic region was not used in the characterization, and therefore all results presented here pertain to a shock-loading condition. The shocked targets were examined using an optical

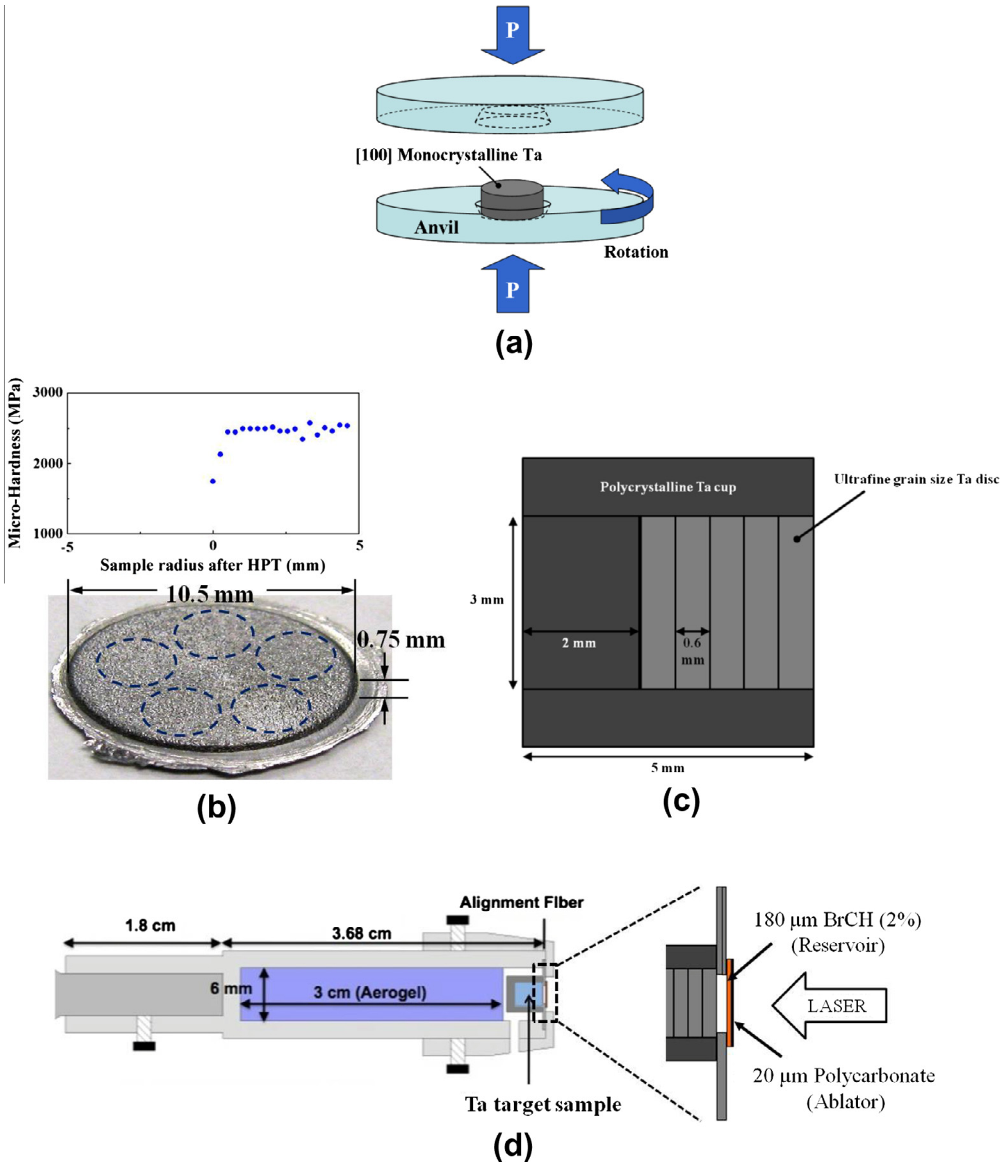

Fig. 1. Tantalum nanocrystalline sample: (a) during high-pressure torsion (HPT); (b) deformed specimen (after HPT) and microhardness across the cross-section; (c) cross-section of Ta target assembly; (d) detailed cross-section of the recovery tube with dimensions.

profilometer (Veeco NT1100), a microhardness tester, a scanning electron microscope (Philips XL30 ESEM) and transmission electron microscopes (TEM, 200 kV). TEM foils were prepared by electropolishing and focused ion beam (FIB, Hitachi NB-5000 FIB-SEM) techniques. The electropolishing liquid, a solution of 87.5 vol.% methanol, 10 vol.% sulfuric acid and 2.5 vol.% hydrofluoric acid, was used at ∼25 V and ∼−35 °C. The temperature was lowered by pouring liquid nitrogen directly into the electropolishing solution. FIB samples were prepared by cutting targets in half along the pulse propagation direction and mounting them into epoxy. They were mechanically polished down to 0.05 µm using $Al_2O_3$ and coated with a thin layer of Ir before the FIB milling procedure. The FIB samples were perpendicular to the shock propagation direction and had thicknesses of 50–100 nm.

## 3. Results and discussion

### 3.1. Pressure estimation and surface cratering

Complementary VISAR experiments were performed on Al–LiF drive calibration samples; they provided interface velocity data that allowed pressure vs. time traces of the loading to be deduced. These VISAR measurements were used to calibrate LASNEX calculations which provide the decay of the pressure as a function of input energy. This information was used as input to the subsequent computer simulations. The 358 and 684 J VISAR results were used to do the calculations. The initial pressure pulse was calibrated using the VISAR traces of the Al–LiF witness plate interface velocity as described by Lu et al. [21]. Fig. 2a shows the interpolated results at energy levels of 200,

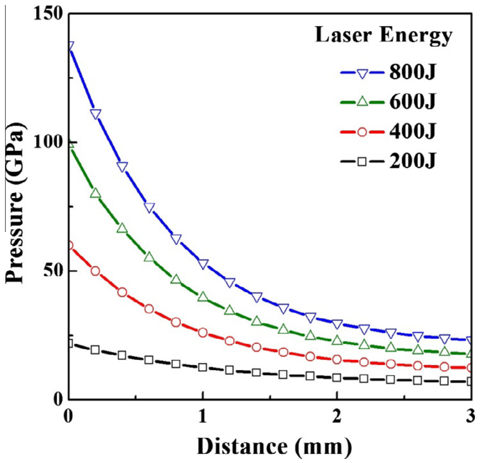

Fig. 2. Pressure profile in material at laser energies of 200, 400, 600 and 800 J obtained through VISAR at two energy levels, LASNEX calculations, and interpolation for values above.

400, 600 and 800 J. This plot provides a rapid means of estimating the pressure at each point within the samples. The LASNEX code is one-dimensional, and therefore the decay of the wave due to radial spreading is not incorporated. Thus, the actual pressures are somewhat lower than the values reported in Fig. 2.

The laser energy deposition produced a significant crater in the specimen surfaces. Figs. 3a and c show the craters under profilometry and SEM. Other than the "blow-off" effect from the laser energy deposition, cracks are also present in the nanocrystalline Ta (Fig. 3d) which is similar to the monocrystalline results (Fig. 3b). By tracking these lines, the general configuration of the cracks was obtained as shown in Fig. 4. For the [100] monocrystalline Ta, a perpendicular pattern of crack lines is formed. The lines present in the nanocrystalline Ta follow a concentric circular pattern. There are two explanations for these cracks. (i) Crack trajectories are thought to form from a ductile-to-brittle transition at high strain rates where the cracks may form by the tensile stresses generated by the large temperature and deformation gradients generated by the laser pulse. (ii) When the reservoir stagnates on the Ta, it melts the first few micrometers. Eventually, the heat dissipates, and this thin liquid Ta layer resolidifies, and contracts in so doing. This contraction during solidification causes the cracks. In monocrystalline Ta, cracks follow {110} planes while there are no specific macroscopic directions/planes in nanocrystalline Ta. Thus, the cracks form perpendicular to the direction of maximum principal stresses, which exhibit radial symmetry.

The cross-section profiles of the crater are inserted in Fig. 5. For calculation accuracy, only the inner crater

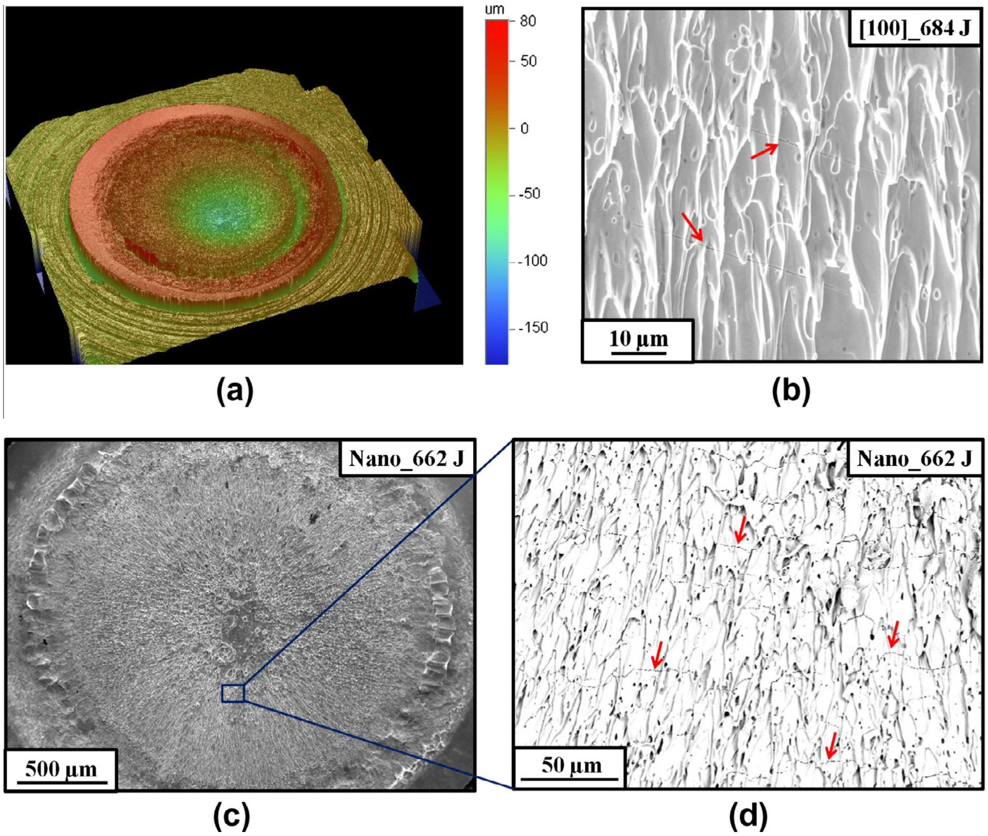

Fig. 3. Surface of Ta after laser compression ($E_{\mathrm{laser}} = 662$ and 684 J): (a) 3-D profilometry; (b) straight crack lines (marked by arrows) observed in [100] monocrystalline Ta traversing the elongated surface features; (c) SEM micrograph of crater in nanocrystalline Ta; (d) back-scattered SEM showing cracks with irregular trajectories in nanocrystalline Ta.

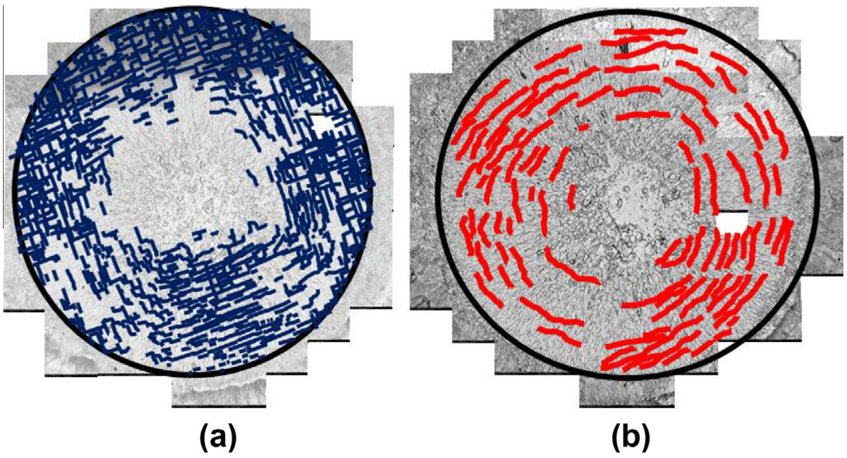

Fig. 4. Tracking crack lines on the crater surface for (a) [1 0 0] monocrystalline Ta (total laser energy 505 J); (b) nanocrystalline Ta (total laser energy 662 J).

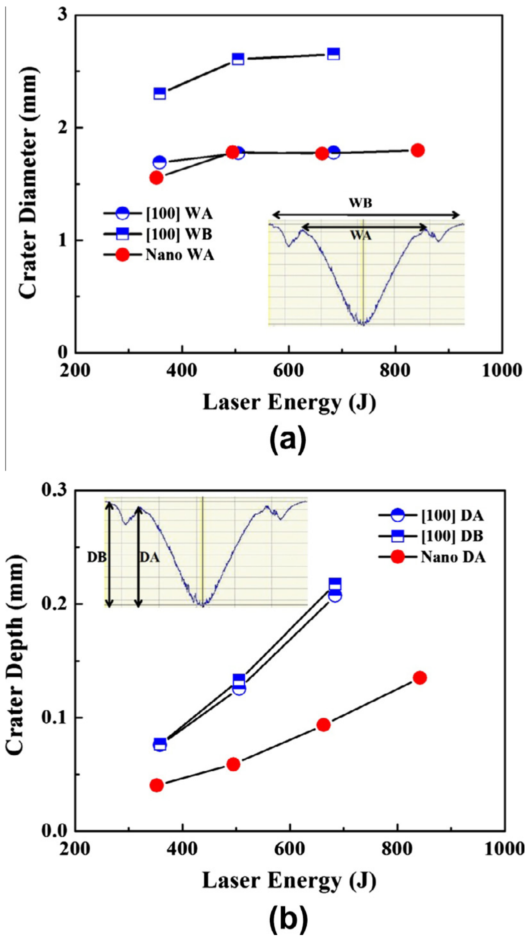

Fig. 5. (a) Diameters and (b) depths of craters formed in [1 0 0] monocrystals and nanocrystals as a function of laser energy.

(WA and DA) was considered. The inner diameter is ~1.8 mm in all cases but the depth is a function of laser energy. Fig. 5 shows plots of the crater dimensions vs. laser energy. From Fig. 5b, it is clear that the crater is deeper for [1 0 0] monocrystalline Ta, which is consistent with its lower strength. Furthermore, there is an essentially linear relationship between crater depth and laser energy.

### 3.2. Microhardness analysis

The shock-recovered [1 0 0] monocrystalline and nanocrystalline Ta targets were sectioned into six and five slices, respectively. Each slice was about 250 μm thick for characterization (Fig. 6a). Microhardness as a function of distance from the energy deposition surface is shown in Fig. 6b for $E_{\text{laser}} = 606$ J [1 0 0] monocrystal

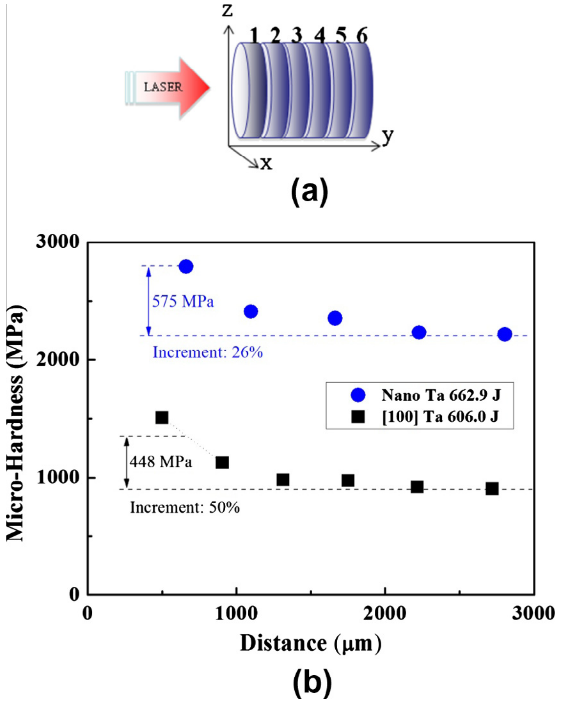

Fig. 6. (a) Slices into which the specimens were cut: each was ~250 μm thick before polishing; (b) microhardness in the region directly under the laser deposition for both [1 0 0] monocrystalline and nanocrystal Ta.

and $E_{\text{laser}} = 662$ J nanocrystal. The microhardness varies across the sample section due to the localization of the laser pulse in the central portion of the specimens [21]. The hardness data presented here all come from the center of each slice. The microhardness decay is most significant in the first millimeter from the compression surface. Nanocrystalline Ta is harder than monocrystalline Ta because of the high strength, expressed by the Hall–Petch equation. It can be seen that the general trend in microhardness decay vs. depth into the sample is the same for both nanocrystalline and monocrystalline Ta. In relative terms, however, the hardness increment under laser compression in nanocrystalline Ta (26%) is only approximately one-half of that for monocrystalline Ta (50%) although the laser energy is 10% higher (Fig. 6b). This is related to the increase in dislocation density, as will become clear in Section 3.3.

### 3.3. Transmission electron microscopy analysis

Characterization by TEM shows the deformation structures associated with the passage of the laser shock pulse. Pre-shock undeformed nanocrystalline Ta structures are imaged in Fig. 7. From the bright-field image. it can be seen that the grain size is ~70 nm. The deformation structures of post-shocked nanocrystalline Ta ($E_{\text{laser}} = 662$ J) taken from slices 1–4 (see Fig. 6a) are imaged in Fig. 8. Fig. 9 shows the Ta ($E_{\text{laser}} = 842$ J) sample taken from the bottom of the crater, indicating the significant grain growth and absence of dislocations in the grains immediately under the crater. Significant grain growth is observed close to the laser impact surface (Figs. 8a and 9). The average grain size, calculated from TEM images in each slice examined, increases gradually when approaching the laser compression surface. An experimentally measured grain size scatter is noted in Fig. 10. Thus, the very large grain size scatter for slice 1 is attributed to the significant growth of some grains at the expense of others. The temperatures induced by laser shocks decay with depth into the sample. The calculated temperature evolution is a function of energy input, and will be discussed in Section 3.3.2.

Few dislocations were observed within the grains of the shocked nanocrystalline sample. Two instances where dislocations were observed are shown in Fig. 11a and b. These two areas are at 1.1 mm (Fig. 11a) and 1.6 mm (Fig. 11b) from the surface. A loose dislocation network can be seen. The measured nanocrystalline dislocation densities were added to the pressure vs. density plot developed by Lu et al. [21] for monocrystalline Ta (Fig. 11c). The calculated dislocation densities in these nanostructure samples is lower than in monocrystalline Ta, which exhibited twins at these pressures, with an associated decrease in dislocation density, discussed by Lu et al. [21]. The dislocation density is significantly lower than anticipated by interpolation from monocrystalline and polycrystalline data. The reason for the lower dislocation densities is the ubiquitous presence of sinks: the grain boundaries. Thus, the dislocations are annihilated after moving distances of the order of the grain size.

#### 3.3.1. Slip–twinning transition analysis

Slip and twinning can be considered as competing deformation processes. The postulation of such a criterion permits an analysis that leads to the predicted transition between the two mechanisms. The slip–twinning analysis, proposed by Meyers et al. [11,12], and applied successfully to the shock compression domain by Murr et al. [33], Meyers et al. [11,12] and Jarmakani et al. [34], predicts the slip–twinning transition for polycrystalline Ta, Cu and Ni, respectively.

Both slip and twinning are driven by shear stress. Hydrostatic compression does not create plastic deformation in cubic metals. Twinning also involves dislocations

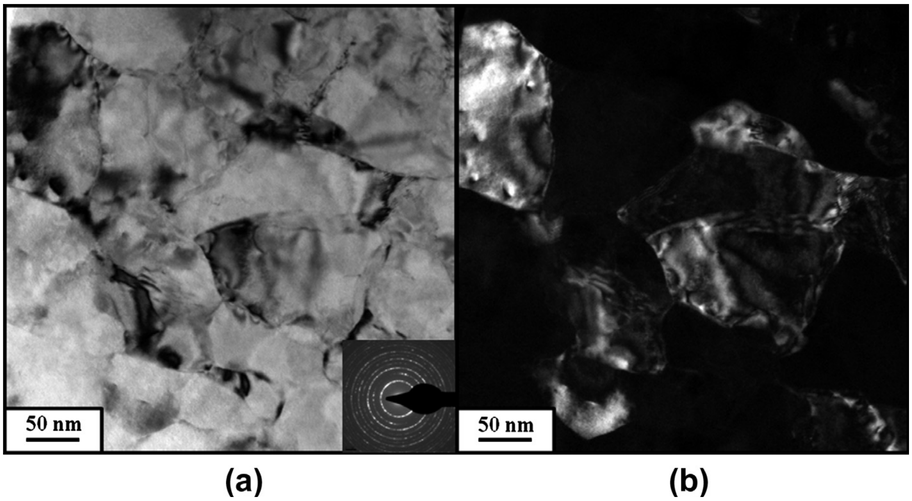

Fig. 7. TEM micrographs for nanocrystalline Ta sample prior to shocking: (a) bright field; (b) dark field. The initial average grain size can be calculated from this series of images and is ~70 nm.

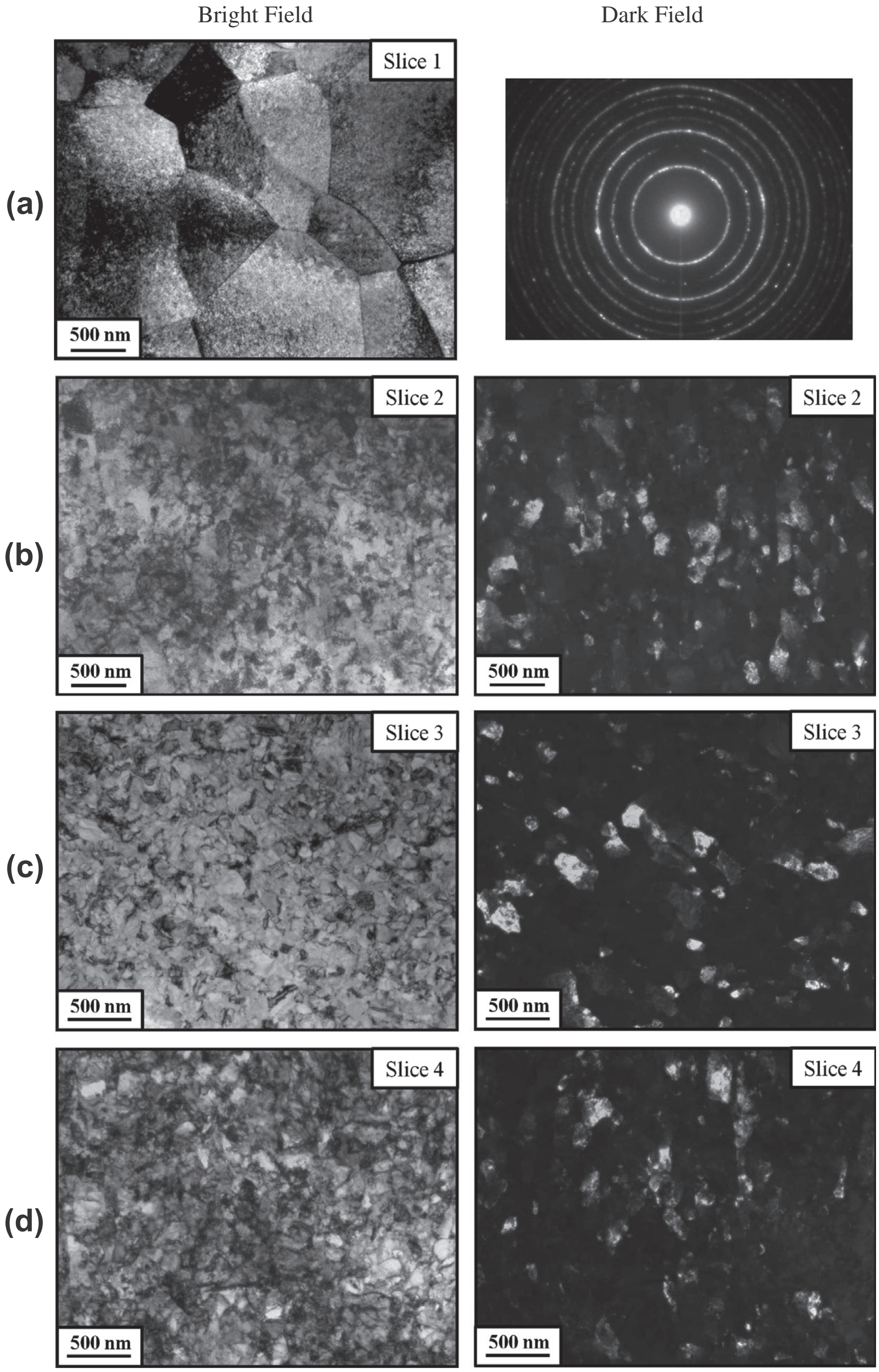

Fig. 8. TEM micrographs as a function of distance from the laser deposition surface for nanocrystalline Ta driven with laser energy of 662 J: (a) slice 1 (~100 μm from the driven surface) and diffraction pattern (for b, c and d); (b) slice 2 (~1100 μm from surface); (c) slice 3 (~1600 μm from surface); and (d) slice 4 (~2200 μm from surface); (left column) bright-field images; (right column of b, c, d) dark-field images.

through the sequential nucleation and propagation of arrays of twinning dislocations:

$$\frac{a}{6}\langle 1\ 1\ 1\rangle = \frac{1}{3}b,$$

where $a$ is the lattice parameter and $b$ is the Burgers vector. For slip, the dislocations are:

$$b = \frac{a}{3}\langle 1\ 1\ 1\rangle.$$

Indeed, shock compression generates a state of uniaxial strain and there are shear stresses and shear strains. The uniaxial strain in the direction of compression can be calculated as a function of pressure. Uniaxial strain (equal to maximum shear strain) can be regarded as a function of shock pressure using values calculated from Rankine–Hugoniot relationship and experimentally obtained equation of state for Ta. For 50 GPa, the uniaxial strain is $\sim -0.2$; for 100 GPa, it is $\sim -0.3$.

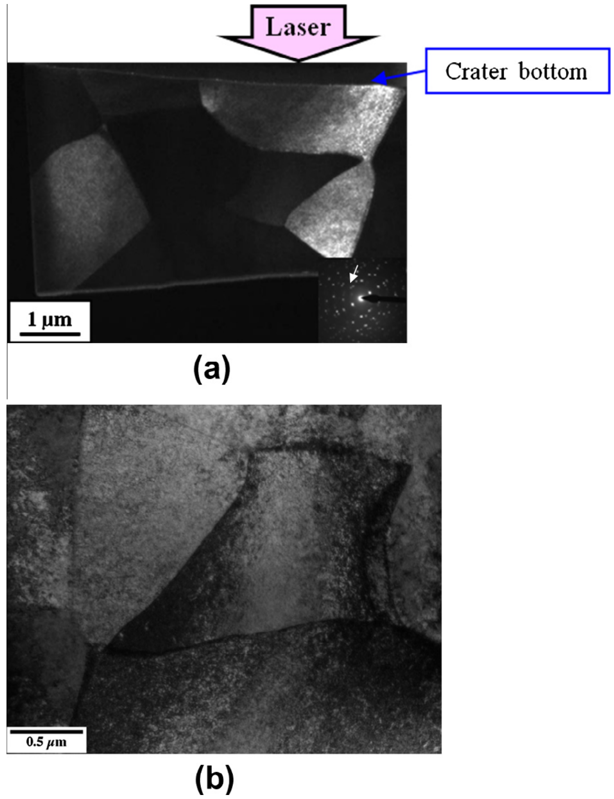

Fig. 9. TEM micrograph at the bottom of the crater with laser energy of 842 J. (a) Dark field of FIB sample with a selected diffraction spot. The selected-area diffraction pattern is quite different from the one in Fig. 7a which shows the nanocrystalline structure. The average grain size is about 2 µm. (b) Bright-field micrograph shows merely dislocations in the grain right under the crater.

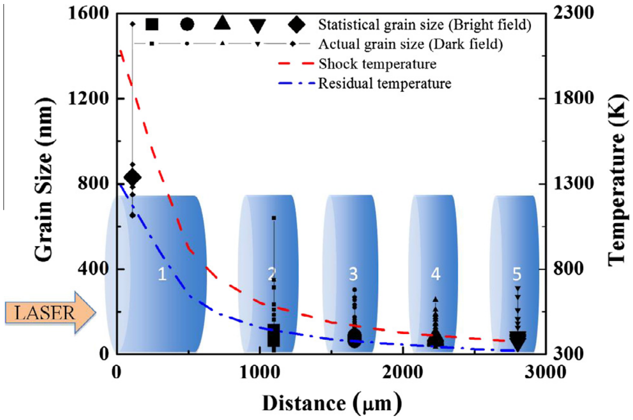

Fig. 10. Grain size and temperature as a function of distance from laser deposition surface in nanocrystalline Ta (total laser energy 662 J). Statistics indicate the average grain size.

The shear stress is related to the shock pressure through [41]:

$$\tau = -\frac{1-2\upsilon}{2(1-\upsilon)}P_{shock}, \tag{1}$$

where $\upsilon$ is Poisson's ratio.

The effect of strain rate on slip can be expressed by the Zerilli–Armstrong (Z-A) equation for bcc metals [35] in the thermally activated region and by the PTW equation [36] in the drag region. This is expressed below by the composite equation whose first term is the Z-A thermal activation regime and whose second term is the PTW drag regime:

$$\sigma_S = \max\left\{(\sigma_S^* + C_2 e^{-C_3 T}\dot{\varepsilon}^{C_4 T} + k_S d^{-1/2})\frac{G(\rho,T)}{G_0(\rho)}, \hat{\tau}_{drag}\right\}, \tag{2}$$

where $C_2$, $C_3$, $C_4$ and $k_s$ are Z-A parameters that have been established for Ta; they are given in Table 1. $\sigma_S^*$ is the athermal stress and $d$ is the grain size, The dynamic experiments by Rittel et al. [37] were used to obtain some of the Z-A parameters given in Table 1; a detailed explanation is provided by Lu et al. [21].

The drag component is expressed as:

$$\hat{\tau}_{drag} = S_0(\dot{\varepsilon}/\gamma\dot{\xi})^{\beta} = \frac{\tau_{drag}}{G(\rho,T)} = \frac{\sigma_{drag}}{2G(\rho,T)} = \frac{\sigma_{drag}}{2G_0(\rho)(1-\alpha T/T_m(\rho))}, \tag{3}$$

where $T_m(\rho)$ is the melting temperature and $\dot{\xi} = c_T/2a$ is the time required for a transverse wave to cross an atom [36]. $G(\rho, T)$ is the density- and temperature-dependent shear modulus, and the other parameters, $S_0 = 0.012$, $\gamma = 0.00004$ and $\beta = 0.23$, are given by Preston et al. [36] for Ta. The graphical expression of Eq. (1) is shown in Fig. 12 for two different grain sizes: 3 and 70 nm.

In previous work [21], the effect of strain rate on twinning was neglected to a first approximation [38]. The twinning stress, $\sigma_T$, has been expressed by Armstrong and Worthington [39] as:

$$\sigma_T = \sigma_0 + m\left(\frac{G(P,T)b}{C_1}\right)^{1/2}\left[\frac{U^*}{RT}\ln\frac{\dot{\varepsilon}}{\dot{\varepsilon}_0}\right]^{1/q} d^{-1/2}, \tag{4}$$

where $G(P, T)$ is expressed by Steinberg [40] as:

$$G(P,T) = G_0\{1 + AP/\eta^{1/3} - B(T-300)\}, \tag{5}$$

with $G_0 = 69$ GPa, $A = 1.45\ \mathrm{GPa}^{-1}$, $B = 1.3 \times 10^{-4}\ \mathrm{K}^{-1}$ and $\eta = \rho/\rho_0$ [14].

The various parameters are given in Table 1.

The onset of twinning corresponds to:

$$\tau_S = \tau_T, \tag{6}$$

where $\tau_S$ and $\tau_T$ are shear stresses. It should be emphasized again that twinning is triggered by the shear stresses and not by the pressure in both conventional and shock-wave deformation.

The strain rate at the shock front increases with the maximum stress. Swegle and Grady [42] proposed a relationship between shock pressure and strain rate that is widely used [33,43]:

$$\dot{\varepsilon} = 27.34 \times P_{shock}^4, \tag{7}$$

where $P_{shock}$ is in units of GPa and $\dot{\varepsilon}$ is in units of $\mathrm{s}^{-1}$.

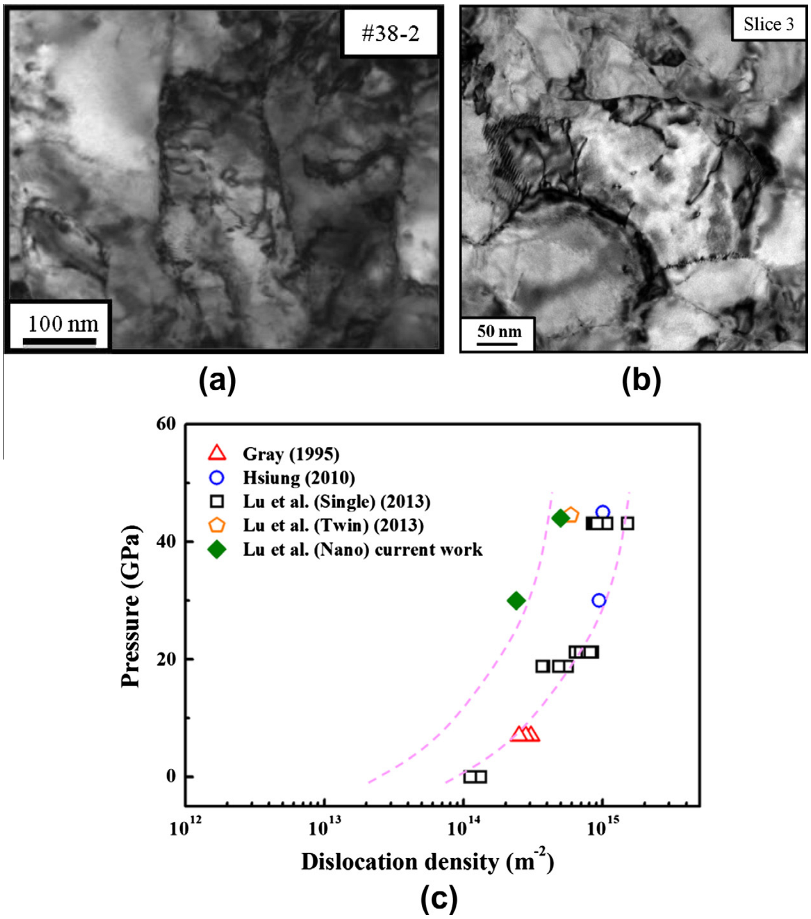

Fig. 11. (a and b) TEM dislocation images in nanocrystalline Ta (total laser energy 662 J): (a) ∼1100 μm from surface; (b) ∼1600 μm from surface. (c) Dislocation density as a function of pressure for different grain sizes and substructures [21].

Applying the Swegle–Grady equation to Eqs. (2) and (4), one can calculate the stresses required for slip and twinning, respectively, as a function of shock pressure. To carry out this analysis, one has to incorporate the effect of the shock temperature, predicted by the Rankine–Hugoniot equations into the formulation. The temperature rise in Ta behind the shock front as a function of shock pressure can be expressed as the second-order polynomial, based on the Rankine–Hugoniot equations (and on the $C_0$ and $S$ values for Ta [41,44]):

$$T_{shock\_Ta} = 0.1007P_{shock}^2 - 1.13P_{shock} + 294.8, \tag{8}$$

where $P_{shock}$ is expressed in units of GPa and $T_{shock\_Ta}$ is in units of K.

The calculations are conducted for both nanocrystalline and monocrystalline Ta and the results are shown in Fig. 13. This analysis predicts the slip–twinning transition pressure for monocrystalline Ta to occur at $P_{shock} \approx 24$ GPa, whereas the transition pressure is above ∼150 GPa for nanocrystalline Ta.

Twinning is experimentally observed at $P_{shock} >$ ∼32 GPa for monocrystalline Ta [21] but is absent in nanocrystalline Ta even at the highest pressure of ∼145 GPa. Thus the modeling predictions are consistent with experimental observations. The α(bcc)–ω(hcp) phase transformation, which requires a higher pressure than twinning (∼68 GPa) in monocrystalline Ta, was not observed in nanocrystalline Ta.

The effect of grain size on the slip–twinning transition pressure for Ta and Ni [41] is shown in Fig. 14. It is evident that the slip–twinning transition pressure is greatly influenced by grain size primarily because of the different Hall–Petch slopes for slip and twinning. The physical explanation for the difference lies in the requirement of high local stresses for the initiation of twinning. These high local stresses can be produced by dislocation pile-ups in monocrystals. In nanocrystals, on the other hand, the large concentration of grain boundaries provides abundant sites at which the shear stresses can be dissipated by dislocation emission.

### 3.3.2. Modeling of temperature profile

In order to calculate the grain growth observed in the vicinity of the energy deposition surface, one has to estimate the post-shock temperature as a function of time throughout the sample. The shock and residual temperature inside the samples can be calculated through [45]:

Table 1
Zerilli–Armstrong, Armstrong–Worthington and shock compression parameters used for the constitutive analysis.

| Parameters | Unit | Value |
|---|---|---|
| $T$ | K | 298 |
| Athermal stress $\sigma_S^*$ | MPa | 20 |
| $C_1$ | $\text{GPa}^{-1}$ | 0.0005 |
| $C_2 = B_0$ | MPa | 1125 |
| $C_3 = \beta_0$ | $\text{K}^{-1}$ | 0.00535 |
| $C_4 = \beta_1$ | $\text{K}^{-1}$ | 0.00024 |
| Tension twin stress | MPa | 370 |
| Compression twin stress $\sigma_0$ | GPa | 0.755 |
| Burgers vector | nm | 0.286 |
| $U^*$ | J | 4.56 |
| $q$ | | 5 |
| $k_s$ | $\text{MPa m}^{1/2}$ | 0.25 |
| $m$ | | 0.236 |
| $R$ | J/mol K | 8.314 |
| $S_0$ (for Ta) | | 0.012 |
| $\gamma$ (for Ta) | | 0.00004 |
| $\xi$ (for Ta) | $\text{s}^{-1}$ | $6.952 \times 10^{12}$ |
| $\beta$ (for Ta) | | 0.23 |
| $T_m$ (for Ta) | K | 3269 |
| $G_0$ | GPa | 69 |
| $A$ | $\text{GPa}^{-1}$ | 1.45 |
| $B$ | $\text{K}^{-1}$ | $1.3 \times 10^{-4}$ |
| $T_0$ | K | 300 |
| $S$ | | 1.2 |
| $\rho_0$ | $\text{g/cm}^3$ | 16.65 |
| $C_0$ | km/s | 3.41 |
| $\gamma_0$ | | 1.8 |
| $C_v$ | J/g K | 0.14 |

$$T_s = T_0 e^{(\frac{\gamma_0}{V_0})(V_0 - V)} + \frac{(V_0 - V)}{2C_v} P + \frac{1}{2C_v} e^{(-\frac{\gamma_0}{V_0})V} \times \int_{V_0}^{V} \left( \frac{C_0^2 (V_0 - V)}{[V_0 - S(V_0 - V)]^2} \right) e^{[(\frac{\gamma_0}{V_0})V]} \cdot \left[ 2 - \left[ \left( \frac{\gamma_0}{V_0} \right) (V_0 - V) \right] \right] dV, \tag{9}$$

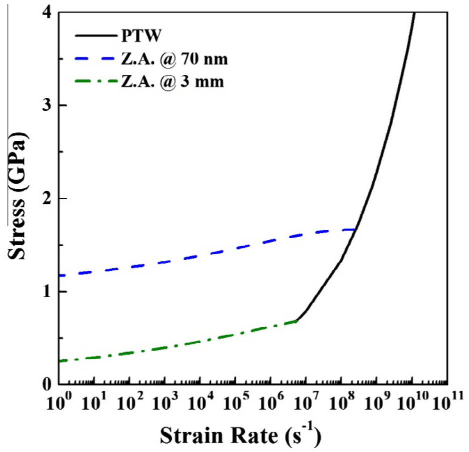

Fig. 12. Slip stresses as a function of strain rate at different grain sizes. Note Z-A thermal activation and the PTW drag regimes. The PTW [36] equation is independent of the grain sizes.

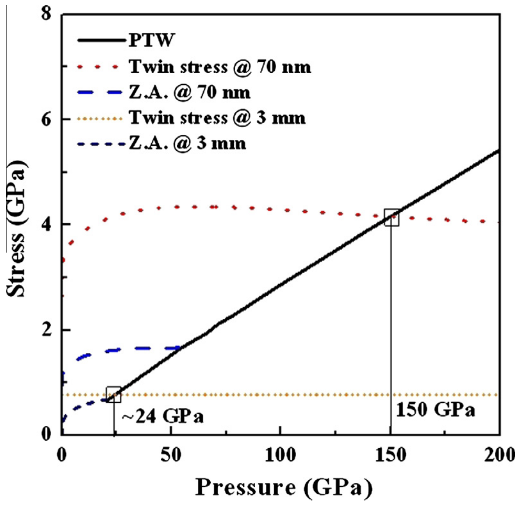

Fig. 13. Slip and twinning stresses vs. shock pressure for Ta with grain sizes of 3 mm (i.e. monocrystalline) and 70 nm. The slip–twinning transition shock pressure is inferred to be $P_{shock} \approx 24$ GPa for monocrystalline Ta and $P_{shock} \approx 150$ GPa for nanocrystalline Ta ($d = 70$ nm).

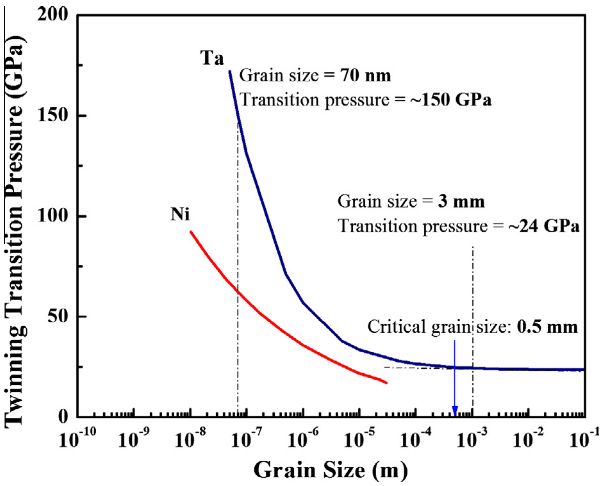

Fig. 14. Calculated twinning transition pressures as a function of grain size for Ni [41] and Ta. The twinning transition pressures are marked for monocrystalline (G.S. = 3 mm, $P = 24$ GPa) and for the nanocrystalline (G.S. = 70 nm, $P = 150$ GPa).

and

$$T_r = T_s \exp\left[ \left( -\frac{\gamma_0}{V_0} \right) (V_0 - V) \right], \tag{10}$$

where $T_0 = 300$ K, $S = 1.2$, $\rho_0 = 16.65$ (g/cm$^3$), $C_0 = 3.41$ (km/s), $\gamma_0 = 1.8$ and $C_v = 0.14$ (J/g K) for Ta. Here, $P$ is the peak pressure of the shock wave and $V$ is the specific volume of the material directly behind the shock which can be calculated from the Rankine–Hugoniot relationships. Based on the results from VISAR (pressure vs. distance), the residual temperature profile throughout the sample subjected to a 684 J pulse immediately after the shock can be calculated. This information is used in Section 3.3.2 in order to calculate the grain growth.

To calculate the temperature variation with time throughout the sample, some assumptions were made: the temperature profile at time $t = 0$ (meaning immediately after the shock has traversed the Ta sample) is shown in Fig. 14; heat conduction is 1-D; the total calculated length for Ta is 5 mm (including 3 mm nanocrystalline Ta and 2 mm bottom momentum trap); the Ta target has uniform and constant thermal properties. The rate of heat transport by thermal conduction is much lower than the shock propagation velocity. This enables the decoupling of the two and leads to the simplified derivation presented here. We assume that, at time $t = 0$, the temperature at each point is equal to the residual temperature. Dividing the sample into N elements with thickness $\Delta x$ and discrete time step $\Delta t$ ($t_m = m\Delta t$), the heat transfer at position $i$ ($1 \leqslant i \leqslant N$) can be calculated [46] as:

$$T_{i,m+1} = T_{i,m} + \frac{\Delta t}{\rho C \Delta x}\frac{k}{\Delta x}(T_{i+1,m} - 2T_{i,m} + T_{i-1,m}), \tag{11}$$

with boundary conditions:

$$\begin{aligned} T_{1,m+1} &= T_{1,m} + \frac{2\Delta t}{\rho C \Delta x}\left[\frac{k}{\Delta x}(T_{2,m} - T_{1,m})\right], \\ T_{N,m+1} &= T_{N,m} + \frac{2\Delta t}{\rho C \Delta x}\left[\frac{k}{\Delta x}(T_{N-1,m} - T_{N,m})\right], \end{aligned} \tag{12}$$

where $k$ is the thermal conductivity ($k = 57.5$ (W/m K)), $C$ is the heat capacity and $\rho$ is the density. Fig. 15 shows the temperature profiles at different positions as a function of time. The temperature change with time at specific distances from the surface is shown in Fig. 15. The temperature has equilibrated to values close to the pre-shock level after 0.1 s. Similar results were reported earlier for Cu [25]. We also can find the temperature change with time at specific distances from the surface as shown in Fig. 15.

### 3.3.3. *Modeling of grain growth*

Grain boundaries have been investigated theoretically using dislocation models since the early 1950s [47]. The interaction between dislocations and grain boundaries has been analyzed by Karduck et al. [48]. The temperature excursion undergone by the metal can lead to grain growth. We use here a simple derivation based on a 2-D model proposed by Hu and Rath [49–53]. It assumes that grain growth is dictated by the grain boundary curvature alone and ignores grain–grain interactions, grain-size distribution, anomalies in curvature and energy effects due to the work-hardened structure. By balancing the forces acting on a curved grain boundary segment, the driving force on the grain boundary can be estimated by the Hu and Rath formulation [49–54], which is described by Gottstein [55].

The total force (per unit length) acting on the grain boundary with grain boundary energy (per unit area) $\gamma_{gb}$ (Fig. 16a) can be obtained from the force equilibrium for a 2-D simplified geometry:

$$F = 2\gamma_{gb}\sin\frac{d\theta}{2}. \tag{13}$$

Considering a small angle ($\sin d\theta \propto d\theta$), the force per area is:

$$\frac{force}{area} = \frac{\gamma_{gb}d\theta}{Rd\theta} = \frac{\gamma_{gb}}{R}, \tag{14}$$

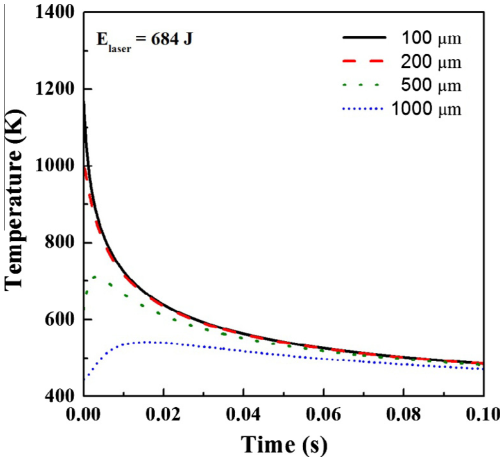

Fig. 15. Temperature as a function of time at different distances from the energy deposition surface: 100, 200, 500 and 1000 μm.

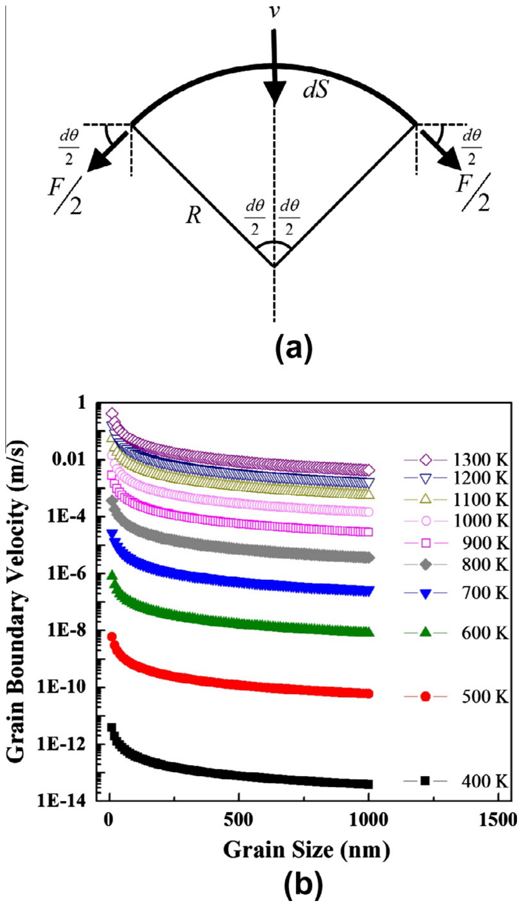

Fig. 16. (a) Schematic showing force per unit length, $F$, acting on the grain boundary with a radius of curvature $R$. (b) Grain boundary velocity as a function of grain size for temperatures varying from 400 to 1300 K (Hu-Rath model [49–53]).

where $\gamma_{gb}$ is the grain boundary energy and $R$ is the radius of the grain (assumed to be spherical). The grain boundary velocity, $v_{gb}$, was assumed by Hu and Rath [49–53] to be proportional to the force acting on the grain boundary segment and can be expressed as [55]:

$$v_{gb} = MF,$$

where $M$ is the grain boundary mobility. Therefore,

$$v_{gb} = \frac{dR}{dt} = M\frac{\gamma_{gb}}{R}. \tag{15}$$

The grain boundary mobility has an Arrhenius-type temperature dependence:

$$M = M_0 \exp\left(\frac{-Q}{kT}\right), \tag{16}$$

where $M_0$ is a rate constant.

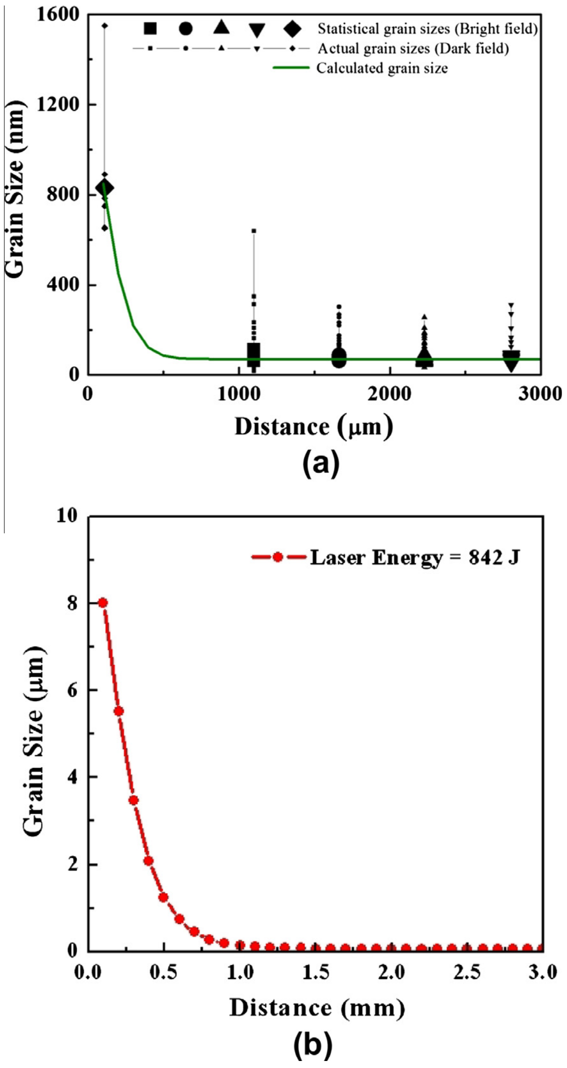

Fig. 17. (a) Measured and calculated grain size as a function of distance from the energy deposition surface (total laser energy 662 J in experiments and 684 J in calculations). (b) Calculated grain size as a function of distance from the energy deposition surface for a laser energy of 842 J.

Combining Eqs. (15) and (16),

$$\frac{dR}{dt} = M\gamma_{gb} = M_0 \exp\left(\frac{-Q}{kT}\right)\frac{\gamma_{gb}}{R}. \tag{17}$$

Separating variables and integrating:

$$\int_{R_0}^{R_f} R\,dR = \frac{1}{2}(R_f^2 - R_0^2) = M_0\gamma_{gb}\int_0^{\infty} \exp\left(\frac{-Q}{kT}\right)dt. \tag{18}$$

Thus, the final grain radius, $R_f$ is:

$$R_f = \left[2M_0\gamma_{gb}\int_0^{\infty} \exp\left(\frac{-Q}{kT(t)}\right)dt + R_0^2\right]^{1/2}. \tag{19}$$

Here, $T(t)$ is the time-dependent temperature. To calculate $R_f$, we need to know $R_0$, $M_0$, $\gamma_{gb}$, $Q$ and $k$. The initial grain size is $2R_0 = 70$ nm and $k = 8.314$ (J/K mol) is the gas constant. The activation energy for boundary migration, $Q$, was determined as 29,200 (cal/mol) for pure Ta from Richards [56]. Wei et al. [57] showed that the grain boundaries in nanocrystalline Ta obtained by HPT are non-equilibrium. According to Nazarov [58], the grain boundary energy in Ta can be estimated as $\gamma_{gb} = 3.2 \times 10^{-2}$ (J/m$^2$). To estimate the constant, $M_0$, the expression for boundary mobility of flexible low-angle grain boundaries [59] and the diffusion coefficient for Ta [60] were used. At 800 K, this gives $M_0 = 5.53 \times 10^{-3}$ m/g for Ta.

Assuming that the grain size is $2R$, the calculated grain boundary velocity as a function of grain size is plotted in Fig. 16b for temperatures of 400–1300 K. When the temperature decreases, the grain boundary velocity decreases dramatically. Therefore, grain boundary movement and grain growth are highly sensitive to the residual temperature. The final grain sizes at different depths in the sample can be calculated from Eq. (19) and these values are plotted in Fig. 17a. The temperatures $T(t)$ are given in Fig. 15 and were obtained by numerical integration. The calculated grain sizes are consistent with experimental results (for $E_{\text{laser}} = 662$ J) and it can be seen that even short cooling times ($\sim$0.1 s) can generate significant grain growth. Fig. 17b shows the calculated grain growth for laser energy of 842 J. From Fig. 9, the average experimentally determined grain size for $E_{\text{laser}} = 842$ J is about 2 μm where the calculated grain size is about 5.5 μm. For $E_{\text{laser}} = 662$ J, the calculated and experimentally measured grain size is the same: $\sim$800 nm. The calculated grain size for $E_{\text{laser}} = 842$ J is 2 μm, much larger than $E_{\text{laser}} = 684$ J, which is consistent with the experimental observations.

## 4. Summary and conclusions

The objective of this research was to establish the effects of shock compression (laser energies between 350 and 850 J) on the structure and mechanical properties of nanocrystalline Ta ($d \approx 70$ nm) and to compare the results with the effects on monocrystalline Ta. The following are the principal findings:

1. The crater depth generated by the laser pulse is a function of laser energy; it is shallower in nanocrystalline Ta than that in monocrystalline Ta, consistent with its higher strength.
2. The principal defects generated by the laser pulse are dislocations. Only a few dislocations were observed in each nanocrystalline Ta grain. The dislocation density is approximately one order of magnitude lower than for monocrystalline Ta, at the same laser energy level.
3. One of the reasons for the low dislocation densities is the profuse availability of dislocation sinks: the nanocrystalline grain boundaries.
4. Constitutive modeling shows that the slip–twinning transition pressure is a function of grain size. This is consistent with the experimental results: twin structures were observed in monocrystalline Ta and absent in nanocrystalline Ta, at the highest characterized laser energy (∼842 J), generating shock pressures of ∼146 GPa.
5. The shock and residual temperatures as a function of pressure were calculated using pressure results obtained by VISAR. The residual temperature profile is expressed as a function of time assuming 1-D heat transfer.
6. Using the Hu–Rath analysis (grain boundary velocity $\propto$ (grain size)$^{-1}$) under a continuously decreasing temperature, the evolution of grain size as a function of time was calculated at different distances from the energy deposition surface. The experimentally measured increase in grain sizes (from 70 to 800 nm for $E_{\text{laser}} = 662$ J and to 2 μm for $E_{\text{laser}} = 842$ J) are explained by calculations based on this mechanism.

## Acknowledgements

This research is funded by the UC Research Laboratories Grant (09-LR-06-118456-MEYM) and the National Laser Users Facility (NLUF) Grant (PE-FG52-09NA-29043). Additional funding was provided by the National Science Foundation of the United States under Grant No. DMR-1160966 (M.K. and T.G.L.) and the European Research Council under ERC Grant Agreement No. 267464-SPDMETALS (T.G.L.). We thank C.T. Wei and Dr. Y. Tang for overall assistance. Electron microscopy was conducted at the SHaRE User Facility, which is sponsored at Oak Ridge National Laboratory by the Division of Scientific User Facilities, US Department of Energy. We also acknowledge the use of the UCSD Cryo-Electron Microscopy Facility which is supported by NIH grants to Dr. Timothy S. Baker and a gift from the Agouron Institute to UCSD.

## References

[1] Askaryan GA, Prokhorov AM, Chanturiya GF, Shipulo GP. Sov Phys JETP-USSR 1963;17:1463.
[2] Ramsden SA, Savic P. Nature 1964;203:1218.
[3] Safonov AN, Grigor'yants AG, Makusheva NA, Sergeev AV. Elektronnaya Obrabotka Materialov 1984;1:26.
[4] Gureyev DM, Zolotarevsky AV, Zaikin AE. J Mater Sci 1991;26:4678.
[5] White RM. Inst Radio Eng Trans Instrum 1962;1–11:294.
[6] White RM. J Appl Phys 1963;34:2123.
[7] Bell CE, Landt JA. Appl Phys Lett 1967;10:46.
[8] Panarella E, Savic P. Can J Phys 1968;46:143.
[9] Skeen CH, York CM. Appl Phys Lett 1968;12:369.
[10] Cottet F, Romain JP, Fabbro R, Faral B. PRL 1984;52:1884.
[11] Meyers MA, Gregori F, Kad BK, Schneider MS, Kalantar DH, Remington BA, et al. Acta Mater 2003;51:1211.
[12] Meyers MA, Schneider MS, Jarmakani H, Kad B, Remington BA, Kalantar DH, et al. Metall Mater Trans A 2008;39A:304–24.
[13] Schneider MS, Kad B, Kalantar DH, Remington BA, Kenik E, Jarmakani H, et al. Int J Impact Eng 2005;32:473.
[14] Remington BA, Allen P, Bringa EM, Hawreliak J, Ho D, Lorenz KT, et al. Mater Sci Technol 2006;22:474.
[15] Kalantar DH, Belak J, Bringa E, Budil K, Caturla M, Colvin H, et al. Phys Plasma 2003;10:1569.
[16] Jarmakani HN, Bringa EM, Erhart P, Remington BA, Wang YM, Vo NQ, et al. Acta Mater 2008;56:5584.
[17] Wang YM, Bringa EM, McNaney JM, Victoria M, Caro A, Hodge AM, et al. Appl Phys Lett 2006;88:061917.
[18] Wei CT, Maddox BR, Stover AK, Weihs TP, Nesterenko VF, Meyers MA. Acta Mater 2011;59:5869.
[19] Wei CT, Nesterenko VF, Weihs TP, Remington BA, Park HS, Meyers MA. Acta Mater 2012;60:3929.
[20] Jamakani H, Maddox BR, Wei CT, Kalantar D, Koniges A, Eder D, et al. Acta Mater 2010;58:4604.
[21] Lu CH, Remington BA, Maddox BR, Kad B, Park HS, Prisbrey ST, et al. Acta Mater 2012;60:6601.
[22] Loomis E, Swift D, Peralta P, McClellan K. Mater Sci Eng A 2005;404:291.
[23] Loomis E. Trans ASME J Eng Mater Technol 2007;129:513.
[24] Peralta P, Swift D, Loomis E, Lim CH, McClellan KJ. Metal Mater Trans A 2005;36A:1459.
[25] Cao BY, Lassila DH, Schneider MS, Kad BK, Huang CX, Xu YB, et al. Mater Sci Eng A 2005;409:270.
[26] Bourne NK. Metall Mater Trans A 2011;42A:2975.
[27] Schuster BE, Ligda JP, Pan ZL, Wei Q. JOM 2011;63:27.
[28] Zhilyaev AP, Langdon TG. Prog Mater Sci 2008;53:893.
[29] DeCarli PS, Meyers MA. Design of uniaxial strain shock recovery experiments. In: Shock waves and high-strain-rate phenomena in metals. New York: Plenum; 1981. p. 341–74 [chapter 22].
[30] Gray III GT. Influence of shock-wave deformation on the structure/property behavior of materials. In: Asay JR, Shahinpoor M, editors. High-pressure shock compression of solids. New York: Springer Verlag; 1993. p. 187–216.
[31] Gray III GT. Shock wave testing of ductile materials. In: Kuhn H, Medlin D, editors. ASM handbook: mechanical testing and evaluation, vol. 8. Materials Park, OH: ASM International; 2000. p. 530–8.
[32] Bourne NK, Gray III GT. Proc R Soc Math Phys Eng Sci 2005;461:3297.
[33] Murr LE, Meyers MA, Niou C-S, Chen YJ, Pappu S, Kennedy C. Acta Mater 1997;45:157.
[34] Jarmakani H, Wang YM, Bringa E, Meyers MA. Shock compression of condensed matter. APS Conf Proc 2007;955:239.
[35] Zerilli FJ, Armstrong RW. J Appl Phys 1990;68:1580.
[36] Preston DL, Tonks DL, Wallace DC. J Appl Phys 2003;93:211.
[37] Rittel D, Silva ML, Poon B, Ravichandran G. Mech Mater 2009;41:1323.
[38] Meyers MA, Voehringer O, Lubarda V. Acta Mater 2001;49:4025.
[39] Armstrong RW, Worthington PJ. Metallurgical effects at high strain rates. New York: Plenum; 1973. p. 401–14.
[40] Steinberg DJ. Equation of state and strength properties of selected materials. LLNL; 1996.

[41] Meyers MA, Jarmarkani H, Bringa E, Remington B. In: Hirth JP, Kubin L, editors. Dislocation in solids, vol. 15. Amsterdam: Elsevier; 2009.

[42] Swegle JW, Grady DE. J Appl Phys 1985;58:692.

[43] Furnish MD, Chhabildas LC, Steinberg DJ. Shock compression of condensed matter. APS Conf Proc 1993;309:1099.

[44] Meyers MA, Murr LE. Shock waves and high-strain-rate phenomena in metals. New York: Plenum Press; 1981.

[45] Meyers MA. Dynamic behavior of materials. New York: John Wiley; 1994.

[46] Kreith F, Manglik RM, Bohn MS. Principles of heat transfer. 7th ed. Cengage Learning; 2011.

[47] Read WT, Shockley W. Phys Rev 1950;78:275.

[48] Karduck P, Gottstein G, Mecking H. Acta Metall 1983;31:1525.

[49] Hu H, Rath BB. Met Trans 1970;1:3181.

[50] Rath BB, Hu H. Met Trans 1969;245:1577.

[51] Rath BB, Hu H. In: Hu H, editor. The nature and behaviour of grain boundaries. New York: Plenum Press; 1972. p. 405–35.

[52] Rath BB, Hu H. Trans TMS-AIME 1969;245:1243.

[53] Rath BB, Hu H. Trans TMS-AIME 1966;236:1193.

[54] Mishra A, Kad BK, Gregori F, Meyers MA. Acta Meter 2007;55:13.

[55] Gottstein G, Shvindlerman LS. Grain boundary migration in metals. Boca Raton, FL: CRC Press; 1999.

[56] Richards DW, Kramer MP, House JW, De Angelis RJ. Int Centre Diff Data 2003;46:285.

[57] Wei Q, Pan ZL, Wu XL, Schuster BE, Kecskes LJ, Valiev RZ. Acta Mater 2011;59:2423.

[58] Nazarov AA, Romanov AE, Valiev RZ. Acta Metall Mater 1993;41:1033.

[59] Winning M, Rollett AD, Gottstein G, Srolovitz DJ, Lim A, Shvindlerman LS. Philos Mag 2010;90:3107.

[60] Vandermeer RA, Snyder WB. Metal Trans A 1979;10A:1031.